

# Comparison of Reconstruction Methods for Free-Space Propagation Phase-Contrast Tomography

Rasmus Dalgas Rasmussen\*, Jakob Sauer Jørgensen\*, Henning Friis Poulsen† and Per Christian Hansen\*

June 10, 2019

## Abstract

Classical reconstruction methods for phase-contrast tomography consist of two stages, namely phase retrieval followed by tomographic reconstruction. Methods that combine these two stages in one regularized optimization problem have recently been suggested. We examine a novel combined regularization method that uses total variation regularized iterative reconstruction technique, which has been suggested in the literature. We compare the combined method with standard two-stage method in simulated free-space propagation experiments with phantoms inspired by materials science. In reconstructions produced by the novel method it is easier to distinguish between similar materials, than in the two-stage methods. A study on reconstruction quality for increasing noise showed that novel method gives significantly better results than the standard method when the noise increases.

## 1 Introduction

Conventional computed tomography (CT) is based on the absorption of X-rays by the objects being analysed. CT is an analysis tool in many applications, for example within materials science, physics, biology and medical imaging. For several of these research areas weakly absorbing objects occur, which will require longer X-ray exposure time and/or an increased number measurements, in order to have the necessary amount of data with low noise. However when X-ray waves pass through an object they are not only attenuated, but the phase of the wave are also shifted due to the material dependent on refractive indices. Phase-contrast tomography (PCT) exploits the phase shift in a more advanced model to improve the reconstruction, compared to using absorption only. This more advanced model can, for weakly absorbing objects, be used to achieve better reconstruction results, than with regular CT.

PCT comes in a series of different experimental set-ups, for an overview of these methods see for example [2]. The set-up we have chosen to focus on here, is

the free-space propagation method, see Figure 1. This experimental set-up is in some sense the simplest set-up since it does not require analyser crystals, gratings or likewise. The set-up is similar to the standard CT scanning set-up, the main differences are some more stringent requirements of the X-ray source and the  $R$ -distance between the object and the detector, which is increased for PCT.

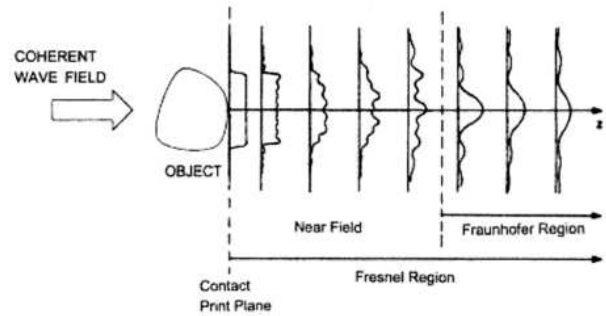


Figure 1: 2D sketch of free-space propagation set-up. Where the intensity for increasing detector distances are illustrated. For free-space propagation the detector will be placed in the near field of the Fresnel region. Taken from [3].

The principle behind free-space propagation PCT is that the phase shift of the X-ray waves is magnified as the distance between the object and the detector  $R$  increases. Based on intensity measurements at the detector, the task is to reconstruct the absorption index and the refractive index decrement of the object. The standard reconstruction process for PCT is a two-stage procedure, a *phase retrieval* stage and a tomographic reconstruction stage. Different phase retrieval methods have been suggested and investigated in the literature. An introduction to, and a comparison of, some of them can be found in [14, 7].

Typically CT reconstructions are carried out by using the filtered backprojection (FBP) method [5]. Regularized reconstruction methods have been examined for standard CT for several applications, Total Variation(TV) regularization has been shown as an advantageous prior for piecewise constant objects [9, 1]. Many objects from materials science which would be desirable to analyse with PCT are piecewise constant objects and we therefore believe that TV-regularization

\*Department of Applied Mathematics and Computer Science, Technical University of Denmark.

†Department of Physics, Technical University of Denmark.

can be valuable in PCT.

Methods that combine the phase retrieval stage and the reconstruction stage have been proposed with different aims. In [3] a filtered backprojection type of algorithm is derived and tested where in [11] an *algebraic* combined model is presented and tested. In [11] promising preliminary results are presented for this new approach and we therefore wish to make thorough comparison between this algebraic combined method and the standard two-stage method.

An Algebraic combined method could allow us to impose regularization to both stages simultaneously, instead of introducing artefacts in one step and regularizing based on these in the next. In [11] it is also suggested that the standard phase retrieval techniques could benefit from using the redundancy within an entire sinogram rather than just being based on the individual projections. With this in mind, it could be presumed that a combined method should be able to produce as good or even better results than the corresponding two stage approach. To examine this hypothesis we have compared the two-stage method with the combined method based on different simulated experiment scenarios and different model variations.

To reduce the complexity of the models and methods the work presented here is based on 2D models, such that the objects are images. All implementations and simulations is carried out in MATLAB.

This report has an introduction, three main sections, 2-4, and finally a conclusion. In section 2 the notation, the physical and mathematical models foundation is briefly introduced. In section 3 the simulated experiments are explained and the reconstruction methods which are to be compared, are presented in more detail. The reconstructed results are presented in section 4, for the two different testing scenarios, one with materials of increasing absorption and one with increasing measurement noise.

## 2 Notation and models

### 2.1 Notation

Vectors and variables are denoted with lower case, e.g.  $u$  or  $\phi$ . Two- and three-vectors are denoted with bold, e.g.  $\mathbf{x}$  or  $\boldsymbol{\omega}$ .

Matrices are denoted with upper case, e.g.  $A$  or  $F$ , and operators with upper case calligraphic letters e.g.  $\mathcal{A}$  and  $\mathcal{F}$ .

The Fourier transform  $\mathcal{F}$  of a one dimensional signal  $f$  is denoted with  $\hat{\cdot}$ :

$$\hat{f}(\omega) = \mathcal{F}(f(x)) = \int_{-\infty}^{\infty} f(x)e^{-2\pi i\omega x} dx. \quad (1)$$

The independent frequency variable is  $\omega$  and the complex unit is denoted as  $i = \sqrt{-1}$ .

The Radon transform  $\mathcal{R}$  of a two dimensional object

$f(x_1, x_2)$  is denoted as:

$$[\mathcal{R}f](t, \theta) = \int_{-\infty}^{\infty} f(t \cos(\theta) - \tau \sin(\theta), t \sin(\theta) + \tau \cos(\theta)) d\tau. \quad (2)$$

Here  $\theta$  is the angular variable and  $t$  is the translational variable, perpendicular to line integration direction, in other words the coordinate variable on the one-dimensional detector.

The line intersection method and discrete linear system for absorption based CT is denoted as

$$Au = b, \quad (3)$$

where system matrix  $A$  with elements  $a_{i,j}$  describes the path length of X-ray  $i$  through pixel  $j$ .  $u$  is a vector with a pixels values and  $b$  describes the intensity measurements. For more details see [9]. The matrix  $A$  can be thought of as a discrete Radon transform operator.

### 2.2 Free-space propagation model

For free-space propagation PCT the measured intensity data in the Fresnel region is related to the material properties through a non-linear propagation model. For material properties  $\delta(x_1, x_2)$ , absorption index, and  $\beta(x_1, x_2)$ , refractive index decrement, the corresponding projections  $B(t, \theta)$  and  $\phi(t, \theta)$ , here called *absorption* and *phase shift*, can be modelled as line integrals along the X-ray propagation [14]:

$$B_{\theta}(t) = \frac{2\pi}{\lambda} [\mathcal{R}\beta](t, \theta), \quad (4)$$

$$\phi_{\theta}(t) = -\frac{2\pi}{\lambda} [\mathcal{R}\delta](t, \theta). \quad (5)$$

Here  $\lambda$  is the X-ray wavelength and  $\mathcal{R}$  is the Radon transform. Based on the absorption and phase shift the measured intensity  $I$  is modelled as the squared absolute value of the convolution of the transmittance  $T$  and the Fresnel propagator  $P^R$ :

$$T_{\theta}(t) = \exp\left(-B_{\theta}(t) + \hat{i}\phi_{\theta}(t)\right), \quad (6)$$

$$P^R(t) = -\frac{\hat{i}}{\lambda R} \exp\left(\frac{\hat{i}\pi}{\lambda R}|t|^2\right), \quad (7)$$

$$I_{\theta}^R(t) = |T_{\theta}(t) \star P^R(t)|^2. \quad (8)$$

Here  $\hat{i}$  denotes the imaginary unit,  $R$  is the distance from the object to the detector,  $|\cdot|$  the absolute value and  $\star$  the convolution operator.

Discretization of the domain and hence the object of interest into  $N \times N$  pixels, gives us discrete versions of the material parameters  $\beta$  and  $\delta$ . A single index notation is introduced  $n = i + (N-1)j$ , for  $i, j = 1, 2, \dots, N$ , so  $n = 1, 2, \dots, N^2$ , and the absorption index and the refractive index decrement are stacked which gives two column vectors,  $\beta_v$  and  $\delta_v$ , with element index  $n$ . Using the discrete Radon transform (3) we define discretized versions of  $B$  and  $\phi$ :

$$B_v = A \left(\frac{2\pi}{\lambda} \beta_v\right) \quad (9)$$

$$\phi_v = A \left(-\frac{2\pi}{\lambda} \delta_v\right) \quad (10)$$

This leads to discrete version of the transmittance and the Fresnel propagator, and from those the intensity:

$$T_v = \exp(-B_v + i\phi_v), \quad (11)$$

$$P_v^R = -\frac{i}{\lambda R} \exp\left(\frac{i\pi}{\lambda R} |t_v|^2\right), \quad (12)$$

$$I_v^R = |T_v \star P_v^R|^2. \quad (13)$$

Here  $\exp$  and  $|\cdot|^2$  denote element-wise operations and  $\star$  denotes the discrete convolution. In practice the discrete convolution is done in Fourier space.

To simulate physical free-space propagation experiments, the forward model introduced above has been implemented, such that intensity measurement can be simulated for:

- a given object: dimensions and material properties,
- a given source: X-ray wavelength and
- given scanning settings: object-to-detector distance, projection angles, detector pixelsize and the number of detector pixels.

Material parameters used are retrieved from [13]. To make the simulated data more realistic, Poisson distributed noise is used to distort the measured intensity. For intensity  $I$  the transmission probability is given  $p = e^{-I}$ . The detector photon counts  $m$  are then sampled from the Poisson distribution with parameter  $pN_0$ , where  $N_0$  is the mean number of photons. The noisy data is then  $-\log\left(\frac{m}{N_0}\right)$ .

### 2.3 Total Variation Regularization

We utilize total variation regularization when solving linear systems such as the reconstruction problem. We formulate the discrete total variation (TV) regularization problem for regularization parameter  $\alpha \in \mathbb{R}^+$  as:

$$u_\alpha = \underset{u}{\operatorname{argmin}} \left\{ \|Au - b\|_2^2 + \alpha \sum_{n=1}^{N^2} \|D_n u\|_2 \right\}. \quad (14)$$

Here  $u$  is a vector of stacked pixel values,  $b$  is the data vector,  $n$  is the pixel-index,  $N^2$  is the total number of pixels, assuming square domain, and  $D_n$  is the local finite difference derivative at pixel  $n$ .

## 3 Reconstruction methods

The free-space propagation PCT reconstruction method of interest is presented. Mathematical models for the two-stage methods and the algebraic combined methods are described, and finally the choice of optimization algorithm and implementation details are explained.

### 3.1 Two-stage method

For absorption CT the measured intensity data can be directly related the material properties, i.e. the attenuation coefficient, by Lambert Beer's law [5, 9]. Since PCT intensity measurements are related to the material properties through a non-linear propagation model, the PCT reconstruction methods typically consist of two stages. The first stage is a phase retrieval stage, where the measured data is processed to achieve what can be interpreted as CT sinogram data. The second stage is a tomographic reconstruction stage, which is closely related to solving the CT reconstruction problem.

Several phase retrieval methods can be found in the literature [14, 4, 7]. We focus on the contrast transfer function (CTF) method, as in [11], since it is a simple linear model. The following models and derivations follows the models presented in [11], [12] and [10]. This method is based on a linearization where low absorption is assumed. The standard CTF method uses measurements from two or even more distances, whereas so called *duality* version is based on a proportionality assumption between the absorption and the phase shift such that single-distance measurements can be used. We have tested both the standard CTF method and duality CTF method, but the results presented in section 4, are restricted to the duality CTF method. This choice is explained in the next section. The CTF method is derived from the expression of the intensity as given in (8). Based on a Taylor expansion of the transmittance function (6), a CTF model that is linear in  $B$  and  $\phi$  can be derived in Fourier space[6]:

$$\widehat{I}^R(\omega) \approx \delta_{\text{Dirac}}(\omega) - 2 \cos(\pi\lambda R|\omega|^2) \hat{B}(\omega) + 2 \sin(\pi\lambda R|\omega|^2) \hat{\phi}(\omega). \quad (15)$$

Here (15) is the standard CTF method in Fourier space, with  $\delta_{\text{Dirac}}$  being the Dirac delta function and  $\omega$  the spatial frequencies. The duality version of the CTF model, with proportionality constant  $\sigma = \phi(\mathbf{x})/B(\mathbf{x})$ , will be:

$$\widehat{I}^R(\omega) \approx [2\sigma \sin(\pi\lambda R|\omega|^2) - 2 \cos(\pi\lambda R|\omega|^2)] \hat{B}(\omega) + \delta_{\text{Dirac}}(\omega) \quad (16)$$

For  $p$  being the size of detector pixel in m, the sampling distance becomes  $F_s = 1/p$  and the Fourier spatial frequencies therefore become  $\omega \in [-\frac{F_s}{2}, \frac{F_s}{2}]$ . Introducing discrete frequency values  $\omega_k$  for  $k = 1, \dots, K$  the CTF method can be formulated as a discrete inverse prob-

lem. The matrices for the CTF method become

$$\psi_k = \pi\lambda R|\omega_k|^2, \quad (17)$$

$$C(R) = \begin{pmatrix} \cos(\psi_1) & 0 & \cdots & 0 \\ 0 & \cos(\psi_2) & \cdots & 0 \\ \vdots & \vdots & \ddots & 0 \\ 0 & 0 & \cdots & \cos(\psi_K) \end{pmatrix}, \quad (18)$$

$$S(R) = \begin{pmatrix} \sin(\psi_1) & 0 & \cdots & 0 \\ 0 & \sin(\psi_2) & \cdots & 0 \\ \vdots & \vdots & \ddots & 0 \\ 0 & 0 & \cdots & \sin(\psi_K) \end{pmatrix}. \quad (19)$$

For a set-up that uses measurements from two distances, the standard CTF method can be presented in a matrix formulation as

$$\begin{pmatrix} \widehat{I}_v^{R_1} \\ \widehat{I}_v^{R_2} \end{pmatrix} = \underbrace{\begin{pmatrix} -2C(R_1) & 2S(R_1) \\ -2C(R_2) & 2S(R_2) \end{pmatrix}}_G \begin{pmatrix} \widehat{B}_v \\ \widehat{\phi}_v \end{pmatrix}. \quad (20)$$

$R_1$  and  $R_2$  are different object-to-detector distances, preferably one close to the object and one further away. For the CTF duality method measurements from a single distance is sufficient, so the resulting matrix system becomes

$$\widehat{I}_v^R = \underbrace{[-2C(R) + 2\sigma S(R)]}_W \widehat{B}_v. \quad (21)$$

The standard PCT reconstruction technique using the CTF method is based on solving two linear systems in two stages. With the standard CTF model the two-stage method would consist of solving (20) for  $\widehat{B}_v$  and  $\widehat{\phi}_v$ , an inverse Fourier transform and finally solving (9) and (10) for  $\beta_v$  and  $\delta_v$ . To distinguish between the different methods we dubbed this method two-stage method using two R-distances, or **TS2R**.

The two-stage method based on the CTF duality method, we call **TSD**. This would consist of solving (21) for  $\widehat{B}_v$ , followed by an inverse Fourier transform and then solving (9) for  $\beta_v$ . Since  $\beta_v$  is assumed to be proportional to  $\delta_v$  for this method, we could easily find  $\delta_v$  as well afterwards.

### 3.2 Algebraic combined method

For this method the term 'algebraic combined' refers to a combination of linear operators. This method was presented in [11]. The operators are in this case matrices describing the discrete Radon transform,  $A$ , the linear phase retrieval methods,  $G$  and  $W$ , and the discrete Fourier transform  $F$ . The Fourier transform is introduced because we can only write up the phase retrieval model as a matrix-operator in Fourier space. The combined model using the standard CTF method in matrix terms becomes:

$$\begin{pmatrix} \widehat{I}_v^{R_1} \\ \widehat{I}_v^{R_2} \end{pmatrix} = G \underbrace{\begin{pmatrix} \frac{2\pi}{\lambda} FA & 0 \\ 0 & -\frac{2\pi}{\lambda} FA \end{pmatrix}}_Q \begin{pmatrix} \beta_v \\ \delta_v \end{pmatrix}. \quad (22)$$

The combined reconstruction method using this model is dubbed algebraic combined method using two R-distances, **AC2R**.

For the duality version of the CTF method it becomes:

$$\widehat{I}_v^R = \underbrace{\frac{2\pi}{\lambda} WFA}_{\text{ACD system matrix}} \beta_v \quad (23)$$

This combined reconstruction method is dubbed algebraic combined duality method, **ACD**.

As for the TS-method presented above the two systems (22) and (23) should be solved as part of the methods.

Testing the four different methods described above, TS2R, TSD, AC2R and ACD, it became clear that solving for  $\delta$  and  $\beta$  simultaneously, would be challenging using a TV-regularization method. The challenge arises due the significant scale difference, between the two indexes, a factor around  $10^3$ . The results become a constant solution for  $\delta$  due to the regularization or a under-regularized solution which is completely dominated by noise. The intention for the AC2R method is to solve for  $\delta$  and  $\beta$  simultaneously, so due these challenges the comparison between the AC2R and TS2R methods is excluded.

### 3.3 Reconstruction method and implementation

When solving the reconstruction problems (9), (10), (22) and (23) we want to impose some regularization on the solutions and we have therefore chosen to formulate the them as TV-regularization problems, as in (14).

For the two-stage methods, TS2R and TSD, the system matrix  $A$  in (9) and (10) is large but sparse, this means that for some problems it can be stored on the memory of standard modern laptop (4 GB ram), though applying it could take up all of this memory. For the combined methods, AC2R and ACD, the Fourier transform  $F$  makes the combined system matrix dense, thus making it infeasible to have in memory. We circumvent the problem by a matrix-free implementation, in which the applications of the forward operator and its conjugate are done without explicitly forming the matrices.

Solving large-scale TV-regularization problems requires efficient first-order algorithms. The Chambolle-Pock (CP) algorithm [15] was shown in [16] to be well suited in the context of CT and implement a matrix-free version to solve (14) for TSD2R/TSD/AC2R/ACD.

The implementation is mainly based on the pseudo-code description listed in algorithm 4 in [16]. In order to speed up the algorithm the implementation has been modified by the adaptive parameter approach presented in algorithm 2 in [8]. This modified approach introduces a primal residual  $p_k$  and a dual residual  $d_k$  of the optimization problem, which are used to adaptively change parameters of the method. As mentioned in [8] the residuals can also be used to define a stopping criterion for the algorithm, since we have that the

primal-dual residual  $\|p_k\|^2 + \|d_k\|^2$  converges to 0 in the CP algorithm i.e.

$$\lim_{k \rightarrow \infty} \|p_k\|^2 + \|d_k\|^2 = 0. \quad (24)$$

Based on experiments using this implemented method, the primal and dual residuals increased within the first 5-10 iterations and afterwards decayed to 0. We introduce a stopping criterion based on reduction of the primal and dual residual. Normalizing by the primal-dual residual in the first iteration as a reference we terminate the algorithm when

$$\xi_k = \frac{\|p_k\|^2 + \|d_k\|^2}{\|p_1\|^2 + \|d_1\|^2} < \tau, \quad (25)$$

for some predetermined tolerance  $\tau$ . In all of our numerical experiments  $\tau$  was set to  $10^{-6}$ .

The implemented large-scale optimization algorithm has been tested and verified against established and reliable optimization software CVX<sup>1</sup>. We note that the general-purpose nature of CVX makes it infeasible for large-scale problems.

### 3.4 Experimental settings

The set up we have presented here allows us to simulate free-space propagation PCT experiments and compare different reconstruction techniques. These simulations have several tunable parameters which could make the number of different experiments grow rapidly. To avoid too many tunable parameters we have limited the simulated experiments to some specific settings, which we believe are realistic for real physical experiments on a laboratory X-ray CT scanner. The chosen parameters are presented in Table 1.

Parameters	Settings
<b>Object:</b>	2D and 200 x 200 pixels
<b>X-ray source:</b>	Energy $e = 40\text{keV}$ , wavelength $\lambda = 0.31\text{\AA}$
<b>Photons:</b>	$N_0 = 10^5$ detected photons per pixel
<b>Distances:</b>	$R = 0.5\text{m}$
<b>Detector:</b>	Pixelsize of $1\mu\text{m}$ , 200 pixels
<b>Projections:</b>	360 angles $\theta \in [0^\circ, 180^\circ[$ , 572 rays

Table 1: Experimental parameters choices.

## 4 Computer simulations

The simulated experiments are inspired by material science, where investigation of material structures on a micro-scale is desired. For polycrystalline materials the micro-scale structures are made up of *grains* of different orientation and material, therefore a phantom with resemblance to a grain-structure consisting of three different materials is introduced. The phantom which is shown in Figure 2, consist of one background

Material	$\beta$	$\delta$
Polycarbonate( $\text{C}_{16}\text{H}_{14}\text{O}_3$ )	$8.43 \cdot 10^{-12}$	$1.64 \cdot 10^{-7}$
Carbon(diamond)	$1.90 \cdot 10^{-11}$	$4.55 \cdot 10^{-7}$
Magnesium	$1.15 \cdot 10^{-10}$	$2.22 \cdot 10^{-7}$
Aluminium	$2.32 \cdot 10^{-10}$	$3.37 \cdot 10^{-7}$
Silicon	$2.68 \cdot 10^{-10}$	$3.01 \cdot 10^{-7}$
Iron	$6.42 \cdot 10^{-9}$	$9.54 \cdot 10^{-7}$
Copper	$9.96 \cdot 10^{-9}$	$1.06 \cdot 10^{-6}$

Table 2: Absorption index ( $\beta$ ) and refractive index decrement ( $\delta$ ) for X-rays of 40 keV of energy for different materials, taken from [13].

material and grains of two different materials, all of which are described by two indexes  $\beta$  and  $\delta$ . If nothing else is mentioned, the background is set to polycarbonate. Indexes for some chosen materials are presented for 40keV X-ray exposure in Table 2.

We compare the two reconstruction methods TSD and ACD, in terms of achievable quality of the reconstructed images. Both methods are used on the same simulated data, with the same optimization algorithm and compared using the same error-measure and visualization in order to make as fair a comparison as possible.

Additional to the settings in Table 1 the duality method requires a qualified guess on a proportionality constant between  $\phi$  and  $B$ , or  $\beta$  and  $\delta$ , called  $\sigma$ . This has for all simulations been chosen as the exact proportionality for the grain material with the smallest  $\beta$ .

The optimization algorithm is run until the stopping criterion with a tolerance of  $10^{-5}$  is met. The regularization parameters have been chosen empirically for each of the simulation in order to achieve the 'best' possible reconstruction. The 'best' reconstruction is in this case measured by two different means: A relative error-measure  $E = \|u^* - u\|_2 / \|u^*\|_2$ , where  $u^*$  is the original, and a visual comparison where sharp edges are favoured. Specific regularization parameter choices are listed together with the reconstructions. The reconstructions are visualized as images where the grey-scale color-range is  $[0.9 \cdot \min(u^*), 1.1 \cdot \max(u^*)]$ . Intensity values outside this range are truncated to the closest value within the range.

We focus on a comparison of TSD and ACD for two scenarios: performance with respect to different materials and performance with respect to noise in the data.

<sup>1</sup> <http://cvxr.com/cvx/>

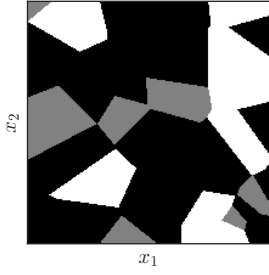


Figure 2: 2D phantom with a background material black, and two different grain materials, gray and white.

#### 4.1 Different materials

The simulated phantom is varied with material ranging from low absorbing material to higher absorbing material, that is from low  $\beta$  to higher  $\beta$ . The two grain materials are chosen such that they have indexes numerically close to each other since distinction between similar materials is the more challenging case in practical applications. Increasing the absorption will violate the low absorption assumption which is part of the CTF model derivation, so higher absorption is also expected to increase the difficulty of the reconstruction problem.

The reconstructions from simulated experiment with materials of increasing absorption index are presented in Figure 3.

For these four experiments the ACD method is generally seen to result in as good or better reconstructions compared to the TSD method, in sense of the error-measure. The TSD results are all visually more blurry and with less sharp edges compared to the ACD results. In the process of choosing the 'best' regularized reconstruction from a series of reconstructions, it became clear that the TSD reconstructions were corrupted by artifacts and/or noise to a higher degree than the ACD reconstructions. On the four TSD reconstructions (3-6) this is what causes the reconstructions to be more blurred, since more emphasis on the regularization term is imposed to compensate for noise and artifacts.

For the low absorbing materials experiments in the first row of Figure 3 both methods give acceptable results where distinction between the different materials is clear. The error measures are also quite low so the reconstruction is good with respect to both the grains and the background.

For the silicon-magnesium and the silicon-aluminium experiments, materials with similar chemical structures is seen to be harder to distinguish as expected. For the silicon-aluminium reconstructions, distinguishing between silicon and aluminium is difficult and methods with measurements from 2 more or more distances would be necessary to get acceptable result.

The experiments with high absorbing materials is highly affected by artifacts, such that distinguishing between background, grain or artifact is difficult. Besides this, edges are also more blurry in the reconstructions.

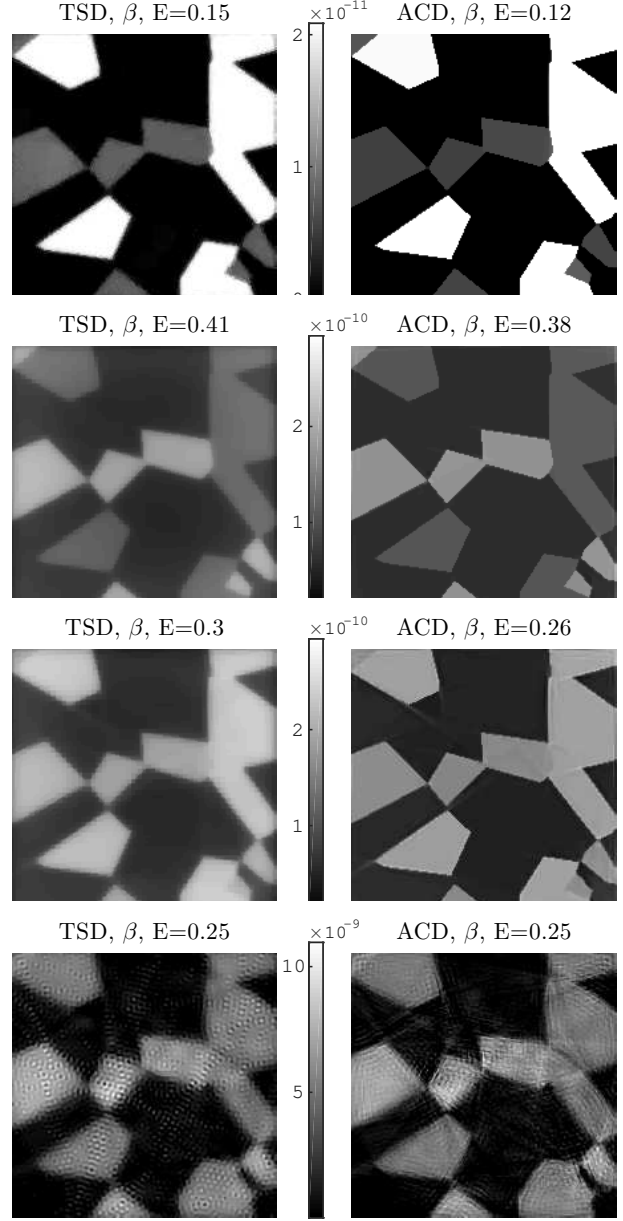


Figure 3: Tests with different materials. First row: non-absorbing and non-refracting background, grains of polycarbonate and carbon in diamond form (highest  $\beta$ ) and Regularization parameters  $\alpha_{TSD} = 0.01$ ,  $\alpha_{ACD} = 120$ . Second row: grains of silicon (highest  $\beta$ ) and magnesium and regularization parameters  $\alpha_{TSD} = 0.1$ ,  $\alpha_{ACD} = 110$ . Third row: grains of silicon (highest  $\beta$ ) and aluminium and regularization parameters  $\alpha_{TSD} = 0.12$ ,  $\alpha_{ACD} = 112$ . Fourth row: grains of copper (highest  $\beta$ ) and iron and regularization parameters  $\alpha_{TSD} = 6$ ,  $\alpha_{ACD} = 5$ .

tions. Error-measures does not tell the same story as the visual inspection, since they are relatively low, this is caused by the background material being correctly reconstructed.

The ACD method was computationally more demanding than the TSD method in the above mentioned experiments. The optimization algorithm needed at least twice as many iterations before the stopping criterion was met. Besides this, the application of the ACD system matrix requires more floating point operations since a Fourier transform has to be calculated each time it is applied. Since this is twice per iteration, each iteration of ACD method is in itself also more computationally demanding than for the TSD method

## 4.2 Increasing noise

To test whether one of the methods, ACD and TSD, is more robust with respect to increasing noise, some experiments are simulated. Since both the ACD method and TSD gave the best reconstructions for the low absorbing materials experiment this is used as an offset for the increased noise experiments. Reducing the number of photons detected at each pixel on the detector will reduce the detected signal and hence increase the noise. From the  $10^5$  detected photons per pixel the number is reduced to  $10^4$  and  $10^3$ , which in practical terms amount to substantial reduction of acquisition time.

The reconstructions from simulated experiment with a decreasing number of recorded photons, and hence increasing noise levels, are presented in Figure 5. The error measure  $E$  is plotted for increasing  $N_0$  in Figure 4.

The TSD reconstructions is seen deteriorate as the noise increases, where the grains of the lowest absorbing material and closest to the center becomes indistinguishable from the background. The edges become more blurry and misclassification of the material of the reconstructed grains is likely to occur. The error measure increases drastically to a limit where the reconstructions are unreliable.

ACD Reconstructions are slightly deteriorated as the noise is increased, though sharp edges, distinguishability between materials and a relatively low error-measure is preserved. This shows that the ACD method is robust to increasing noise. For the high noise problems, the polycarbonate grains are hard to visually distinguish from the background, but numerically the difference is still clear and a simple thresholding segmentation would yield a low ( $< 2\%$ ) pixel misclassification.

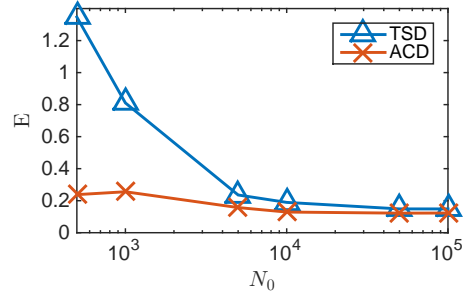


Figure 4: Relative reconstruction error  $E$  for increasing number of photons  $N_0$ , i.e. decreasing noise on the data.

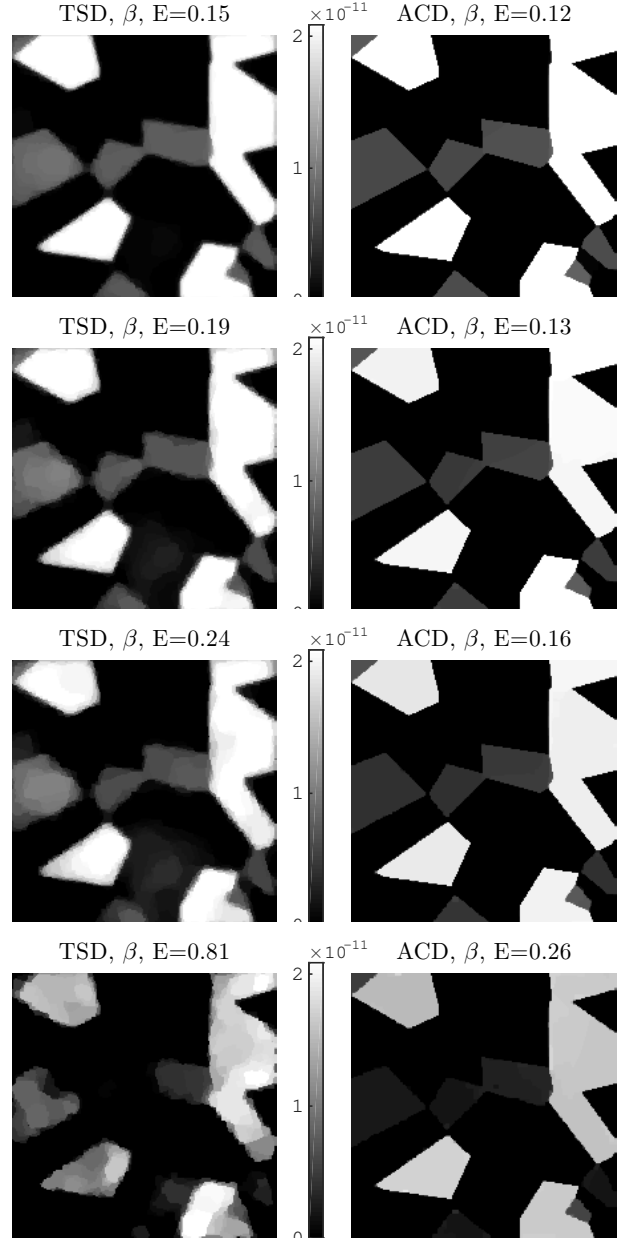


Figure 5: Tests for increasing data noise, i.e. decreasing number of photons  $N_0$ . Non-absorbing and non-refracting background. Grains of polycarbonate and carbon i diamond form (highest  $\beta$ ). First row  $N_0 = 5 \times 10^4$ , second row  $N_0 = 10^4$ , third row  $N_0 = 5 \times 10^3$  and fourth row  $N_0 = 10^3$ .

## 5 Conclusion

Simulated PCT experiments have served as a basis for a comparison between two different PCT reconstruction methods, a classical two stage method and a newer algebraic combined method which has been suggested in the literature. The simulated experiments are modelled to follow real experiments to a high degree, such that the data the methods are tested on is realistic, but still related to a known ground truth.

A visual comparison between the TSD and ACD method showed an advantage of using the ACD method for materials with increasing absorption since they were less affected by noise, but in terms of the error-measure, they were similar.

For the increasing noise experiments, the TSD method had problems handling data with high noise, [Figure 5](#), whereas the ACD method was still able to reconstruct the phantom with a relatively low error-measure and sharp edges. For practical applications where a reduction of the acquisition time is needed, the ACD method could therefore be a useful reconstruction method.

The ACD method was more computationally demanding than the TSD method, so for reconstruction problems with only low noise or low requirements to sharp edges in the reconstruction, the standard TSD method would be preferable, due to efficiency.

Total variation regularization is related to a prior expectation of the solution to be piecewise constant, so for this to be an optimal choice of regularization method the objects should be piecewise constant. Besides this assumption on the object, the results in this report are also restricted to the CTF phase retrieval method. Other phase retrieval methods such as the TIE (transport of intensity) phase retrieval method could also be examined, in order to see if the ACD method would be advantageous in this situation. Besides this some future work could be to apply the ACD method to real data which is corrupted by noise and see if the same conclusions could be drawn.

## 6 Acknowledgements

This work is part of the project HD-Tomo funded by Advanced Grant No. 291405 from the European Research Council.

## References

- [1] J. Bian, J. H. Siewerdsen, X. Han, E. Y. Sidky, J. L. Prince, C. a. Pelizzari, and X. Pan. Evaluation of sparse-view reconstruction from flat-panel-detector cone-beam CT. *Phys. Med. Biol.*, 55(22):6575–99, Nov. 2010.
- [2] A. Bravin, P. Coan, and P. Suortti. X-ray phase-contrast imaging: from pre-clinical applications towards clinics. *Phys. Med. Biol.*, 58(1):R1–35, Jan. 2013.
- [3] A. V. Bronnikov. Theory of quantitative phase-contrast computed tomography. *J. Opt. Soc. Am. A*, 19(3):472, 2002.
- [4] A. Burvall and U. Lundström. Phase retrieval in X-ray phase-contrast imaging suitable for tomography. *Opt. Express*, 19(11):6355–6367, 2011.
- [5] T. M. Buzug. *Computed Tomography - From Photon Statistics to Modern Cone-Beam CT*. Springer Berlin Heidelberg, 2008.
- [6] P. Cloetens, W. Ludwig, J. Baruchel, D. Van Dyck, J. Van Landuyt, J. P. Guigay, and M. Schlenker. Holotomography: Quantitative phase tomography with micrometer resolution using hard synchrotron radiation x rays. *Appl. Phys. Lett.*, 75(19):2912, 1999.
- [7] J. R. Fienup. Phase retrieval algorithms: a comparison. *Appl. Opt.*, 21(15):2758–69, Aug. 1982.
- [8] T. Goldstein, E. Esser, and R. Baraniuk. Adaptive primal-dual hybrid gradient methods for saddle-point problems. *arXiv Prepr. arXiv1305.0546*, 2013.
- [9] J. S. Jørgensen. *Sparse Image Reconstruction in Computed Tomography*. PhD thesis, 2013.
- [10] A. Kostenko. *Phase-contrast x-ray tomography for soft and hard condensed matter*. PhD thesis, 2013.
- [11] A. Kostenko, K. J. Batenburg, A. King, S. E. Offerman, and L. J. van Vliet. Total variation minimization approach in in-line x-ray phase-contrast tomography. *Opt. Express*, 21(10):12185–96, May 2013.
- [12] A. Kostenko, K. J. Batenburg, H. Suhonen, S. E. Offerman, and L. J. van Vliet. Phase retrieval in in-line x-ray phase contrast imaging based on total variation minimization. *Opt. Express*, 21(1):710–23, Jan. 2013.
- [13] S. Kuznetsov. X-ray optics calculator, 2014. [http://www.ipmt-hpm.ac.ru/xcalc/xcalc/ref\\_index.php](http://www.ipmt-hpm.ac.ru/xcalc/xcalc/ref_index.php), IMT RAS, Chernogolovka, Russia, [Retrieved May 20 2014].
- [14] M. Langer, P. Cloetens, J.-P. Guigay, and F. Peyrin. Quantitative comparison of direct phase retrieval algorithms in in-line phase tomography. *Med. Phys.*, 35(10):4556, 2008.
- [15] T. Pock and A. Chambolle. Diagonal preconditioning for first order primal-dual algorithms in convex optimization. *2011 Int. Conf. Comput. Vis.*, pages 1762–1769, Nov. 2011.



- [16] E. Y. Sidky, J. H. Jørgensen, and X. Pan. Convex optimization problem prototyping for image reconstruction in computed tomography with the Chambolle-Pock algorithm. *Phys. Med. Biol.*, 57(10):3065–91, May 2012.